Separating Particulate Matter from a Single Microscopic Image

Tushar Sandhan and Jin Young Choi
Department of ECE, ASRI, Seoul National University, South Korea
tushar@snu.ac.kr, jychoi@snu.ac.kr

Abstract

Particulate matter (PM) is the blend of various solid and liquid particles suspended in atmosphere. These submicron particles are imperceptible for usual hand-held camera photography, but become a great obstacle in microscopic imaging. PM removal from a single microscopic image is a highly ill-posed and one of the challenging image denoising problems. In this work, we thoroughly analyze the physical properties of PM, microscope and their inevitable interaction; and propose an optimization scheme, which removes the PM from a high-resolution microscopic image within a few seconds. Experiments on real world microscopic images show that the proposed method significantly outperforms other competitive image denoising methods. It preserves the comprehensive microscopic foreground details while clearly separating the PM from a single monochromatic or color image.

1. Introduction

Microscopic imaging allows visualization of subcellular structures at various levels of resolution with unprecedented accuracy. It has become a vital source of visual data for biologists and widely used as a primary tool in research and medical assistance. It grants us a new vision for scrutinizing miniature details and thereby fulfilling inquisitiveness of the human mind.

However, presence of particulate matter (PM) in the atmosphere causes hindrance to the microscopy. PM is the blend of various solid and liquid particles suspended in atmosphere with diameters larger than 10 nm and smaller than 50 μm [39]. Comparing the size of PM with perceptible day-to-day objects, it becomes transparent or a mild scattered noise (e.g. haze) for general purpose photography. That is as the PM concentration in an atmosphere increases, the visibility decreases. On the other hand PM settles over the glass slide or objective lens of the microscope, where it becomes comparable in size with the specimen. So in microscopic imaging, PM acts as an obstacle rather than just a scattered noise. Final microscopic image is rendered often with undesired superposition of the true object (foreground) and the ultra-fine unwanted PM (background). Here we address the ill-posed problem of foreground and background separation to produce a clean microscopic image as shown in the Figure 1.

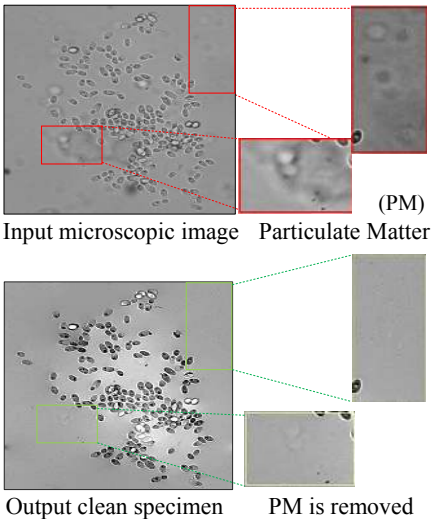

Figure 1: Top: input image of the yeast colonies is contaminated by undesirable particulate matter (PM). Bottom: our method separates PM to produce a clean specimen.

Microscopic image data acquisition has significant challenges like proper staining of the specimen, sustaining certain humidity and surrounding temperature, maintaining appropriate illumination to reduce photo toxicity, preventing background clutter and separating overlapping nuclei [16, 24, 43, 64]. So there is scarcity of microscopic labeled data [67]. Each image contains significant number of objects such as nuclei, cells or neurons, so availability of just few hundreds of microscopic images produces thousands of data points, which is enough to train the learning based algorithms such as deep neural networks (DNN) for detection, segmentation or classification tasks [2, 23, 52, 61, 62, 63]. However for image denoising, each image serves as a single datum and there is often absence of a ground truth e.g. an underlying clean image.

Thus it is necessary to resort to a non-learning based method for enhancing the microscopic images.

Microscopic images of crystals or tissues exhibit periodic or quasi-periodic texture, so significant visual information will be concentrated within certain spots observed in frequency domain [6]. So band-pass filtering, Gabor filtering, curvelets and wavelet-based multiscale analysis have proved to be effective for denoising in high-resolution transmission electron microscopy [14, 22, 27, 28, 60]. Unlike tissues, bacterial colonies do not always grow homogeneously [30], which limits the effectiveness of these transform domain filtering methods.

Microscopic images are often acquired at low light to reduce photo-toxicity of living cells [10], which induces extra noise and subcellular components lose their fine details i.e. resolution [32]. These problems are alleviated to some extent by changing the microscopic acquisition process, such as long exposure image capture without a photo-damage [7, 13, 42, 49]. Contrast enhancement methods [9, 31] also work equally well for uniform illumination and uniform background, but fail in non-ideal circumstances. For example histogram equalization methods introduce color distortions and are not robust in dealing with uneven illumination conditions [15, 66].

Degradation of microscopic images has been tackled by modeling the noise. In case of additive white Gaussian noise, NL-means filter has given efficient and simple solution for noise reduction while preserving the image geometry [8, 32]. For Poisson noise assumption, denoising is achieved by exploiting the image redundancy via patch-based representation, principal component analysis, total variation denoising and dictionary learning methods [12, 21, 37, 50, 51]. These methods are effective when the size of PM is extremely small as compared to specimen i.e. PM behaves as a noise rather than an obstacle.

Integrated microscope allows simultaneous data acquisition from multiple optical imaging modalities [44, 58, 68]. Multimodal microscopy co-registers multiple images to leverage the benefits from multiple structural and functional mechanisms [59,68], so it can reduce the background noise. However high-cost and bulkiness restrict their wide usage.

Artifact disentanglement network [40,41] removes metal artifacts from clinical CT scan images; multimodal unsupervised image-to-image translation (MUNIT) [26] and diverse image-to-image translation (DRIT) [34,35] are disentangled representation frameworks which learn how to do a translation between two image modalities from the unpaired training data. In our case PM and Specimen are the two modalities but abundant training data is not available.

We present detailed study about physical properties of the PM and its interaction with the microscopic imaging system, which helps to translate this domain knowledge into suitable image priors. To simultaneously address the data scarcity and image denoising problem in the microscopy, we formulate a non-learning based optimization scheme.

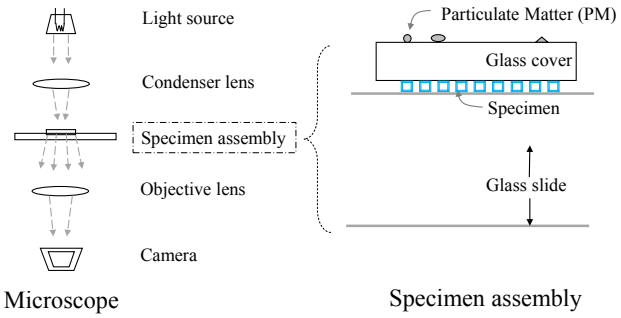

Figure 2: Left side shows conventional microscopic imaging process and basic components of the microscope. On the right side, specimen assembly is shown in detail, where the PM needlessly obstructs optical path in the microscope.

2. Our Approach

To understand the image degradation process, we first outline the principles of microscopy, then examine properties of the PM and its unavoidable interaction with the components of a microscope.

2.1. Microscopic imaging

There are various kinds of microscopes, however basic microscopic assembly and imaging concept can simply be outlined like in Figure 2. It consists of a mainly monochromatic light source for illuminating the specimen to acquire lucid visual data, a condenser lens to focus the light onto the specimen, a glass slide and cover slips for holding the specimen, an objective lens for image magnification and finally CCD or CMOS sensors for digitally acquiring the visual data [4]. To avoid any loss of the visual data, the pixel pitch of these sensors is kept smaller than the minimum resolvable distance decided by the magnifying objective lens [11]. Thus even the slight presence of PM nearby specimen assembly, which is exposed to nearby surroundings, will also be captured in the final image. Occasionally an eyepiece is used at the last stage for further magnification and directly viewing the specimen.

2.1.1 Low illumination

Low sensitivity sensors (low ISO settings) are used in bright light photography which in turn helps to reduce the background noise, because the obstructing effect of PM is overshadowed by the overwhelming visual information available from the true object due to higher illumination [19]. Specimen under microscopy is biological living organisms

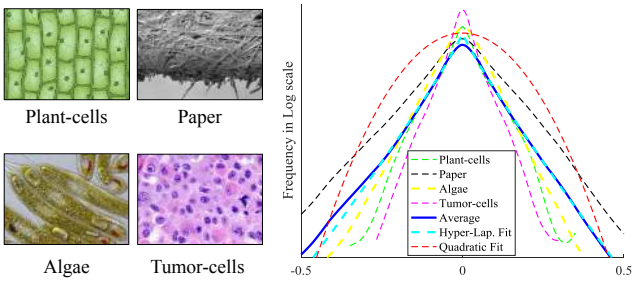

Figure 3: Left side: Typical clean microscopic images (top row: plant-cells, paper; bottom row: algae, tumor-cells). Right side: Their gradient statistics. Average statistics is better approximated by hyper-Laplacian with $\alpha = 0.8$, whereas quadratic or Gaussian approximation is unfit.

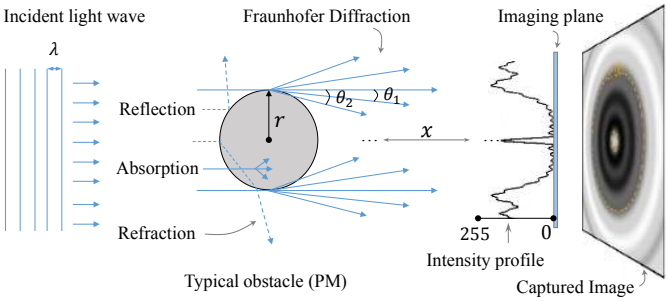

Figure 4: Incident light wave interacts with the spherical obstacle and it gets refracted, reflected, absorbed and diffracted before reaching the imaging plane. Intensity profile in the final captured image shows a smooth variation.

or reactive medical compounds. So to avoid living cell damage, photo-bleaching or photo-reactions [47], the irradiating photon budget is restricted in the microscopy and sensors need to be operated at higher sensitivity which is susceptible to background noise or the PM. Microscopic imaging with these constrained resources, produces noisy visual data in the presence of background PM.

2.1.2 Specimen assembly

Specimen assembly as shown in Figure 2 consists of an object (i.e. specimen) placed over a thick glass slide and covered with a thin glass from the top. It protects the specimen from an accidental contact and dust by sealing it from the surrounding environment. A liquid stain is added over the specimen to better highlight the individual features of the living cell. The cover slip is about 100 to 200 μm thick, it keeps the substrate in a flat or an even thickness and protects it from oxidation or evaporation [54].

2.1.3 Gradient statistics of the specimen

General real-world images exhibit sparse spatial gradient statistics [38, 53]. In Figure 3, we analyze the gradient distributions for representative microscopic images, which are mostly free from background clutter by the PM. It validates that average gradient statistics of clean microscopic images is nicely approximated by hyper-Laplacian distribution, whereas quadratic or Gaussian distribution is far from the fit. So we model the distribution for specimen S as,

$$P(\nabla S) = \prod_{i \in \mathbb{I}} \frac{1}{w_1} \exp\left(-\frac{1}{\sigma_1} \sum_{\partial_j \in \mathbb{J}_S} |(\partial_j * S)_i|^{\alpha} \right), \quad (1)$$

where scalars w_1, σ_1 are normalizing weight and spread respectively, i is the pixel index $\in \mathbb{I} = \{1, \cdots, N\}$, $*$ is the convolution operator, and the derivative filters ∂_j belonging to the set $\mathbb{J}_S = \{[1, -1], [1, -1]^T\}$ and $\alpha = 0.8$.

2.2. Particulate matter

PM is categorized as coarse particles with a diameter between 2.5 and 10μm (PM_{10}) and fine particles with a diameter up to 2.5μm ($PM_{2.5}$) [29] and larger PM is up to size 50 μm [39]. The major constituents of PM_{10} and larger particles are organic compounds, metal oxides, pollen grains, dust and sea salt, whereas $PM_{2.5}$ includes ultra-fine pollutants like hydrocarbons, nitrogen and sulfur oxides etc. [1].

It is difficult to maintain cleanliness standards like semiconductor workstations in research laboratories or at daily work. Moreover microscopic imaging is also carried out in outdoor conditions, so the interaction between specimen assembly and the PM is inevitable. What if one wipes out specimen assembly to remove the PM before microscopy? Wiping process initiates the triboelectric effect, where specific material becomes electrically charged and attracts the nearby particles upon the frictional contact. That is why LCD screens, window glasses are commonly covered with a thin dusty layer. Glass and the constituents of PM_{10} are further apart in the triboelectric series [55]. So it even speeds up the settlement process of coarse PM on the specimen assembly (see Figure 2 right part). It is necessary to maintain certain humidity nearby the specimen assembly to avoid the osmolarity changes [16], and PM particles are hygroscopic which can cause further reduced visibility or noise [3].

2.2.1 Translucency of the PM

Size of the PM is well within few multiple orders of the wavelength λ of the light source (Figure 2), and they are obstructing the optical path (section 2.2). So as λ is comparable with the obstacle size, the diffraction of light is prominent and even if the PM is much larger, the diffraction arises from its edges, as shown in Figure 4. As light is not com-

pletely obstructed, the hindrance from PM in microscopic imaging becomes translucent.

Considering the Fraunhofer diffraction at the contour of the PM in near forward direction [56], the total intensity $I(\theta_n)$ as a function of forward angle θ_n is given by,

$$I(\theta_n) = \frac{I_0}{2k^2x^2}\alpha^4\left\{\frac{\mathcal{J}_1(\alpha \sin\theta_n)}{\alpha \sin\theta_n}\right\}^2, \tag{2}$$

where diffraction order is n, input illumination is I_0, $k = \frac{2\pi}{\lambda}$ is a wave number, distance between the PM and the imaging plane is x, $\mathcal{J}_1()$ is the Bessel function of the first kind of order unity and $\alpha = \frac{2\pi r}{\lambda}$ is the dimensionless size parameter. This model does not depend on optical properties of the obstacle, hence it is applicable to the PM which is a mixture of different objects having variety of shapes.

For a spherical obstacle as in Figure 4, the diffraction gets traced into concentric rings of intensities, whose radii depend upon the PM size [45, 57]. From (2) the acquired intensity is inversely proportional to the square of the separation x between PM and the imaging plane. According to Figure 2, the PM is farther from the imaging plane as compared to specimen by the amount of thickness of the cover slip (sec. 2.1.2). So their intensity drops very quickly and patterns become blurrier than specimen.

Considering the zeros of the $\mathcal{J}_1()$, we can derive that the radius of low intensity concentric ring R is inversely proportional to the obstacle size i.e. $R \propto \frac{1}{r}$. Thus diffraction is noticeable for smaller objects like PM, whereas for larger ones like specimen it is non-evident.

Thus due to translucency and smooth variation of the intensity around the edges of PM, we model gradient statistics for the background PM with the Gaussian-like distribution,

$$P(\nabla B) = \prod_{i\in\mathbb{I}} \frac{1}{w_2} \exp\left(-\frac{1}{\sigma_2^2}\sum_{\partial_j\in\mathbb{J}_B} \|(\partial_j * B)_i\|^2\right), \tag{3}$$

where σ_2 is the standard deviation, w_2 is a normalizing weight and $\mathbb{J}_B$ is the set of second order derivative filters $\mathbb{J}_B = \{[1,-2,1], [1,-2,1]^T\}$.

2.3. Optimization

Microscopic image I is formed via superposition of PM as a background B and the specimen S (sec. 2.1) i.e. $I = S + B$. Being a linear operator, this composition is valid in gradient domain as well. We decompose these layers by maximizing the joint probability, i.e. equivalently minimizing $-\log P(\nabla S, \nabla B)$. Sections 2.1 and 2.2 indicate that S and B are independent, additionally they cannot be more intense than the actual image $(S, B \leq I)$ and should be non-negative $(0 \leq S, B)$; with slight algebraic manipulation on $-\log()$ function and substituting $B = I - S$, we obtain the energy minimization problem as,

$$\min_S \sum_{j\in\mathbb{J}_S} |\nabla_j S|^\alpha + \frac{\gamma}{2}\sum_{j\in\mathbb{J}_B} \|\nabla_j S - \nabla_j I\|^2$$
$$\text{s.t. } \forall i \quad 0 \leq S_i, B_i \leq I_i. \tag{4}$$

The cost function in (4) is non-convex as $\alpha < 1$, so we use half-quadratic splitting technique [20, 33] to solve (4) iteratively. It requires objective function to be separable, hence we introduce an auxiliary variable Y which splits the cost in (4) as,

$$\min_{S,Y_j} \sum_{j\in\mathbb{J}_S}\left\{|Y_j|^\alpha + \frac{\beta}{2}\|\nabla_j S - Y_j\|^2\right\} + \tag{5}$$
$$\frac{\gamma}{2}\sum_{j\in\mathbb{J}_B}\|\nabla_j S - \nabla_j I\|^2 \quad \text{s.t. } \forall i \;\; 0 \leq S_i, B_i \leq I_i.$$

At each iteration t the positive weight β increases and as $\beta \to \infty$, the problems (4) and (5) become equivalent. We solve (5) by iteratively updating the variables as described in the following.

Solving Y. Discarding the variables unrelated to Y gives,

$$Y_j^{(t+1)} = \underset{Y_j}{\text{argmin}}\left\{|Y_j|^\alpha + \frac{\beta}{2}\left\|Y_j - \nabla_j S^{(t)}\right\|^2\right\}. \tag{6}$$

The (6) is solved independently for each pixel i, so it is a single variable optimization which can be speedily solved with the help of a lookup table (LUT) [33]. We map 10^3 values from $\nabla_j S^{(t)}$ to Y_j within a range -0.5 to 0.5 in the LUT. This range is chosen as the average gradient distribution from Figure 3 is bound within this range. The missing values from LUT are interpolated on demand.

Solving S. After fixing Y, the (5) becomes quadratic in S. It can be easily solved by differentiating with respect to S and equating to 0. As manipulation involves intensive image gradients or filtering, we apply 2D FFT $\mathcal{F}$ for fast recovery of S as,

$$S^{(t+1)} = \mathcal{F}^{-1}\left(\frac{\gamma\sum_{j\in\mathbb{J}_B}\overline{\mathcal{F}\nabla_j}\odot\mathcal{F}\nabla_j\odot\mathcal{F}I + \beta\sum_{j\in\mathbb{J}_S}\overline{\mathcal{F}\nabla_j}\odot\mathcal{F}Y_j^{(t)}}{\gamma\sum_{j\in\mathbb{J}_B}\overline{\mathcal{F}\nabla_j}\odot\mathcal{F}\nabla_j + \beta\sum_{j\in\mathbb{J}_S}\overline{\mathcal{F}\nabla_j}\odot\mathcal{F}\nabla_j + \epsilon}\right) \tag{7}$$

where $\mathcal{F}\nabla_j$ is the optical-transfer function or the Fourier transform of the j^{th}derivative filter kernel from the set $\mathbb{J}_B$ or $\mathbb{J}_S$; and $\overline{\mathcal{F}\nabla_j}$ is its complex conjugate. A small scalar $\epsilon = 10^{-8}$ is added for avoiding division by 0. In (7) the final division and the product $\odot$ is performed element-wise.

Satisfying constraints. We impose the constraints in (7) at each iteration t via addition of a normalizing constant κ to all pixels in $S^{(t)}$, such that $0 \leq \kappa + S^{(t)} \leq I$. There is no

Algorithm 1 Clean specimen layer recovery

Input: input microscopic image I; optimization weight γ; total number of iterations T
Initialize: $S^{(0)} = I,\ \beta = \beta_0$
for iteration t from 1 to T **do**
    update $Y_j^{(t)}$ using (6)
    recover $S^{(t)}$ using (7)
    update $S^{(t)} = \kappa + S^{(t)}$ using (8)
    close the gap between (4) and (5) via $\beta = 2\beta$
output: clean specimen image $S = S^{(T)}$

penalty if $\kappa + S^{(t)}$ falls within bounds, but there should be a fixed penalty once it disobeys the constraints. Thus using an unit-step function $\mathcal{U}()$ we find suitable κ by minimizing the loss function (8) with a gradient descent update,

$$\min_{\kappa} \sum_{i \in \mathbb{I}} \mathcal{U}\big(\kappa + S^{(t)} - I\big)^2 + \mathcal{U}\big(-\kappa - S^{(t)}\big)^2. \quad (8)$$

We summarize this iterative optimization process in the Algorithm 1, where at $t = 0$ the specimen layer is initialized with the input microscopic image $S^{(0)} = I$. Our experiments showed that approximate $T = 6$ iterations are sufficient to arrive at a good solution.

3. Experiments

In this section, we describe the implementation details and the experimental setup. The effectiveness of the proposed approach is verified through sets of experiments and comparisons with the state-of-the-art image denoising methods using real-world as well as synthetic inputs. All our results for the clean microscopy (i.e. denoised specimen images), including the one in Figure 1, are obtained by using Algorithm 1 without any further image post-processing.

Dataset. We have constructed a new dataset with significant 500 real-world and synthetic microscopic images. They are of diverse genre including medical (*e.g.* drugs, tumor cells with or without stains *etc.*), biological (*e.g.* bacterial cultures, yeast growth in brewing process *etc.*) and artificial objects (*e.g.* salt crystals, carbon nano-structures *etc.*); which are captured at low to high-illumination with different thickness of the cover slip (section 2.1). Considering photo-toxicity for living cells [47], only artificial objects were captured at very bright illumination. Dataset includes monochromatic and color images of resolution from 300×400 to high-resolution 1920×1920. To help reproducibility, this dataset as well as our Matlab implementation will be publicly available for download.

Implementation. Algorithm 1 was implemented in Matlab without any GPU usage, where empirically we have set $\beta_0 = 20$, $\gamma = 300$ and rational behind the values of other parameters has already been given in the section 2.

Competitive methods	Clean microscopy PSNR	SSIM
Lefkimmiatis (UDNet) [36]	10.91 dB	0.8658
Homomorphic filtering [46]	11.70 dB	0.5898
CLAHE (Contrast manipulation) [69]	13.24 dB	0.8114
Xu *et al.* (TW sparse coding) [65]	10.90 dB	0.8785
Fu *et al.* (Underwater Enh) [17]	13.28 dB	0.3733
Ren *et al.* (Multiscale ConvNet) [48]	13.25 dB	0.6600
Fu *et al.* (Fusion Enh low light) [18]	11.84 dB	0.8802
Berman *et al.* (Non-local method) [5]	14.00 dB	0.6444
Ours (Iterative optimization)	18.56 dB	0.9501

Table 1: Quantitative comparison with various methods. In each column, top three values are color coded as RGB respectively; and the rows satisfying PSNR >10dB as well as SSIM > 0.80 are displayed with a gray background.

3.1. Quantitative comparisons

Using the empty specimen assembly (sec.2.1.2), an image of the PM alone can be obtained at that specific time and configuration. Due to requirement of the ground truth (GT) for quantitative comparisons, we have synthesized the input microscopic image (shown in Figure 5a) by mixing an approximate clear specimen image with the PM. We also made sure that, the appearance of the synthetic input resembles to that of real-world microscopic images having natural contamination from the PM as shown in Figure 6a.

For validating the effectiveness of the proposed method, we extensively compare it with the various relevant methods shown in Table 1. As discussed in section 1, we have selected the recent methods for comparative analysis namely, DNN based learning approach Universal Denoising Networks (UDNet) [36], homomorphic filtering to reduce multiplicative noise [46], Contrast Limited Adaptive Histogram Equalization (CLAHE) [69], Trilateral Weighted Sparse Coding (TWSC) real-world image denoising scheme [65], underwater image enhancement method [17], non-local [5] and DNN [48] based approach for image dehazing and the fusion based low-light enhancement technique [18].

The results are compared using both the peak signal-to-noise ratio (PSNR) and structural similarity index (SSIM) [25], because being a global measure, PSNR does not account for local variation between images; whereas SSIM is perceptual metric which quantifies structural visual quality degradation. Thus quantitatively better denoising methods are those which simultaneously produce high PSNR and SSIM. These are highlighted with gray background of the rows in Table 1 and visually analyzed further in Figure 5. Among contrast manipulation methods, we chose CLAHE [69] for further visual analysis as it showed some better results on real-world inputs (Figure 6).

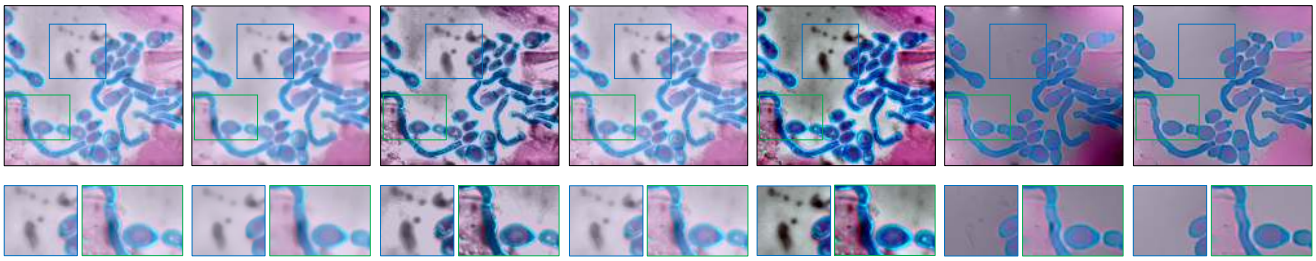

10.87 dB 0.8559	10.91 dB 0.8658	13.24 dB 0.8114	10.90 dB 0.8785	14.00 dB 0.6444	18.56 dB 0.9501	← PSNR ← SSIM
(a) Synthetic	(b) UDNet [36]	(c) CLAHE [69]	(d) TWSC [65]	(e) Dehaze [5]	(f) **Ours**	(g) Ground truth

Figure 5: Quantitative comparisons are performed using a synthetic image in (a). The results of various methods are shown from (b) to (f) columns, which are then compared with the ground truth (g) to obtain the corresponding PSNR and SSIM values. Image regions affected with the PM are highlighted using bounding-boxes and enlarged at the bottom of each image.

Underwater image enhancement method by Fu *et al*. [17] has achieved good PSNR at 13.28 dB however drastically failed to attain any reasonable SSIM. Similarly the dehazing methods [48] and [5] showed high PSNR but low SSIM. Underwater environment and the haze, share similar photo-characteristics of diffused illumination due to intense light scattering effect. So these methods are specifically tailored towards discovering the visual data hidden under uniformly diffused and scattered illumination. However for microscopic imaging, as discussed in section 2.2.1, the artifacts are generated mainly from the light diffraction from the PM. Thus dehazing like image enhancement methods collectively produced low SSIM. We chose only the non-local dehazing method [5], a slightly better performing method among them for more visual comparisons in Figure 5 and 6.

Figure 5 visually analyzes results of the important competitive methods from Table 1. Image regions containing the evident artifacts from the PM are highlighted using colored bounding boxes, which are then enlarged at the bottom of corresponding image. UDNet [36] being a universal denoising method, reduces the whatever Poisson noise present in the microscopic imaging, as shown in Figure 5b, and improves PSNR to 10.91 dB along with SSIM to 0.8658. However localized acute noise due to the PM remains unharmed. Sparse coding based denoising approach (TWSC) [65] attempts further in reducing the PM noise but barely scratches it out as shown in the cropped region at the left bottom of Figure 5d and produces slightly better 0.8785 SSIM.

Dehazing [5] improves contrast of the input image a lot to obtain high PSNR till 14 dB, but disturb the original color consistency and in-fact enhance the PM noise; so it offers low 0.6444 SSIM in Figure 5e CLAHE [69] more or so does the same thing but in moderation, so image composition is not largely diverged from the GT and produce 0.8114 SSIM (Figure 5c) which is lower than the input (Figure 5a).

As our method appropriately modeled the diffraction effects from PM and the highly sparse gradient statistics of specimen, it has successfully reduced the PM noise along with preserving structural and color composition of the underlying true image. Our method does not change any contrast or luminance of the input image. It is solely developed for the purpose of preserving underlying true information of the specimen with reducing the PM artifacts. From the cropped regions at the bottom of Figure 5f, we can clearly see that the PM is almost disappeared. So quantitatively it achieves significantly higher 18.56 dB PSNR and 0.9501 SSIM for cleaning the microscopic images.

3.2. Comparisons on the real-world images

Figure 6 shows the qualitative results of various denoising methods on real-world important microscopic images, which are of varying resolution, illumination, specimen content and the process of capture e.g. stained vs non-stained microscopy. We also include the real-world images gathered from online sources in our experimentation for effectively verifying the ubiquitous presence and undesirable side effects of PM in the microscopy. We have included additional experimental results on real-world microscopic images and minute details about the proposed method in the supplementary material.

Figure 6 serves an important reference for the qualitative microscopy imaging analysis, where the denoising results on each input from 6a by competitive methods are shown in 6b to 6f. Average time taken by them to process all inputs from 6a is shown in the last row of Figure 6 and discussed in section 3.3. Important regions containing the PM and some part of the specimen are highlighted using colored bounding boxes, which are zoomed in at the bottom of each image for better visualization. In the following paragraphs we provide the comparative analysis for each row of the Figure 6.

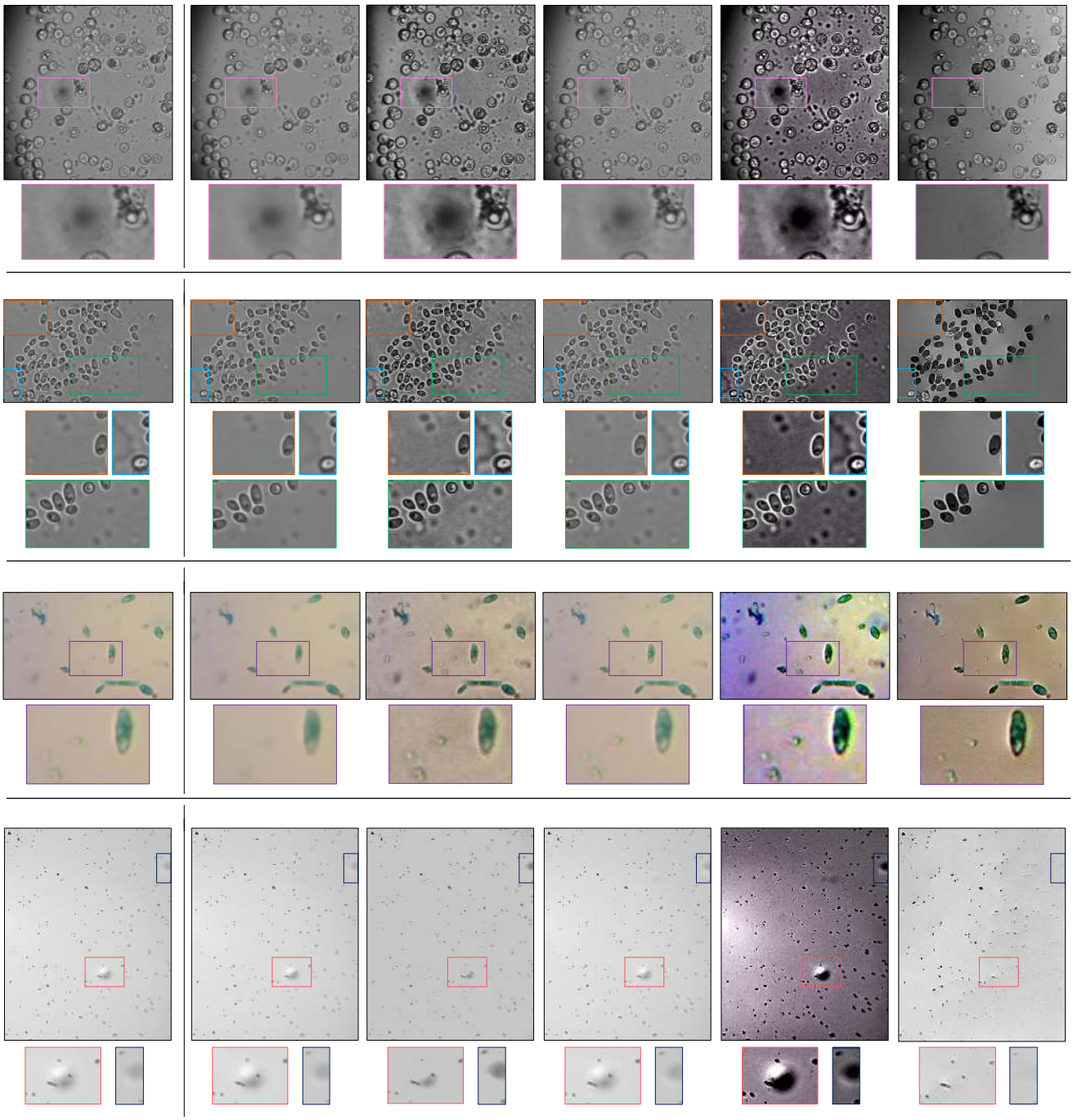

Proc. time →	5.93 sec.	0.48 sec.	513.2 sec.	2.64 sec.	5.52 sec.
(a) Inputs ↑	(b) UDNet [36]	(c) CLAHE [69]	(d) TWSC [65]	(e) Dehaze [5]	(f) **Ours**

Figure 6: Qualitative comparison using various kinds of real-world microscopic images. Specific regions are high-lighted using colored bounding boxes and their enlarged versions are also shown at the bottom of each image. 1st row: Brewing process is captured under microscope at low and non-uniform illumination, where the noise due to PM is significant. 2nd row: Image before formation of the yeast colonies at low but uniform illumination. 3rd row: Bacterial image using cell staining process for acquiring better contrast of the cell parts. 4th row: Artificial sub-micron particles at very bright illumination, where artifacts due to the PM are still present. Bottom row shows an average computation time for processing all the inputs.

First row in Figure 6 shows the brewing process captured at non-uniform and low illumination, where the artifact due to PM (highlighted and shown in the inset) resembles other circular shapes in the specimen but differently shows the mild fringing pattern i.e. diffracted first ring like in Figure 4. As our method explicitly characterizes this phenomenon, it precisely separates the PM without affecting the nearby specimen (Figure 6f). UDNet [36] greatly reduced just the speckled noise, TWSC [65] kept input almost unaltered; whereas CLAHE [69] and Dehaze [5] amplified the artifacts by enhancing contrast of the image.

Second row in Figure 6 presents the image of yeast cells at low but uniform illumination to avoid any unforeseeable cell damage possibly due to photo-bleaching [16]. Low light causes Poisson noise to peek in the system. Additionally it also includes the PM artifacts of different sizes and structures, as highlighted by the red, green and blue bounding boxes *e.g*. dispersed spiny structure of the PM is shown in the blue box (smallest cropped inset). So this image serves an excellent reference for investigating the globally diffused and locally acute microscopic noise. In red or top-left inset, the noise is mostly globally diffused where UDNet [36] showed the best denoising results (followed by TWSC [65]) without affecting contrast or brightness of the original image; whereas our method reduced the global noise with the expense of slightly altering the brightness; and contrary CLAHE [69] and Dehaze [5] significantly altered the specimen by amplifying both noise and brightness. Blue or the smallest inset shows the locally acute PM artifact which is enhanced further by CLAHE [69] and Dehaze [5] as shown in Figure 6c and 6e. UDNet [36] has slightly reduced it and TWSC [65] has completely ignored it whereas our method has completed removed it without damaging the adjacent yeast cells. Green or the largest inset contains mixed (global and local) noise, where our method performed the best followed by UDNet [36].

Third row in Figure 6 depicts the biological image of isolated bacilli-form bacteria obtained using microscopic staining, which offers better contrast for highlighting the various cellular matter. It is clean specimen image and almost free from noise or any significant PM artifacts. It is used here to compare and check any potential side effects of the denoising methods on a clean specimen. Cropped image region in an inset below shows a fully grown large bacterial cell with few other tiny cells. TWSC [65] and CLAHE [69] have preserved the original content as it is, however UDNet [36] has mistakenly removed the tiny specimen cells considering them as noise. Our methods has slightly altered contrast near the cell walls however original specimen information is kept intact. Dehaze [5] has drastically changed the color consistency but has preserved all the structural cell information, which is the most important requirement in microscopy *i.e*. to preserve true underlying data.

Fourth row in Figure 6 portrays artificial sub-micron particles (diameter $3\mu m$) imaged at very bright illumination as there is no light irradiance constraints for non-living and non photo-reactive specimen. Artifact due to the PM is still present even at this bright illumination, which is shown in red or large inset below the image; and a mild dark noisy spot is shown in the small inset. Interestingly at bright illumination, CLAHE [69] has not altered the contrast drastically, moreover it has reduced the bright noisy spot. As the global speckled noise is absent at a higher illumination, UDNet [36] and TWSC [65] have just kept input image unmodified. Dehaze [5] has not only enhance the bright noisy spot but also has introduced additional non-uniform illumination in the output. Our method has clearly spotted bright and dark artifacts due to PM, and comfortable removed them to produce the clear specimen image.

So overall our method arguably produce the best results as shown in Figure 6f across all illumination, specimen type, various shape and sizes of the PM. It removes globally diffused as well as locally acute noise without sacrificing the true underlying specimen details.

3.3. Processing time

Using the authors provided implementations executing in an identical computational environment, average processing time for all the methods is reported in the Figure 6. Though CLAHE [69] and Dehaze [5] methods are much faster, according to their qualitative results they are far from usability in the microscopic image denoising. UDNet [36] and TWSC [65] took approximately 6 and 500 seconds respectively. The proposed method produces the best results within a decent average time about 5.5 seconds per image, as FFT and LUT based quick iterations help it to handle high-resolution images quite well in an optimization.

4. Discussion

We have proposed the scheme for automatic separating the particulate matter (PM) from a single high-resolution microscopic image. We have thoroughly analyzed the physical properties of the PM, microscopic image acquisition process and their inevitable interaction which causes hindrance in the microscopic imaging. Thereby translating domain knowledge into the appropriate image priors, we have formulated a non-learning based optimization scheme for simultaneously addressing the data scarcity and image denoising problem in the microscopy.

Our method approximates the diffraction patterns of PM and exploits the disparity of gradient statistics between specimen and the PM. Its iterative solution based on FFT and LUT is quite stable and faster than other off-the-shelf optimization solvers. We hope that this work along with collected dataset will help researchers to gain insight into the vast array of microscopic imaging affairs.

References

[1] Kate Adams, Daniel S. Greenbaum, Rashid Shaikh, Annemoon M. van Erp, and Armistead G. Russell. Particulate matter components, sources, and health: Systematic approaches to testing effects. *Journal of the Air and Waste Management Association*, 2015. 3

[2] S. Albarqouni, C. Baur, F. Achilles, V. Belagiannis, S. Demirci, and N. Navab. Aggnet: Deep learning from crowds for mitosis detection in breast cancer histology images. *IEEE Trans. Med. Imag.*, 2016. 1

[3] The world bank. Air pollution in ulaanbaatar: Initial assessment of current situation and effects of abatement measures. In *Sustainable Development Series: discussion*, 2009. 3

[4] M. Bass. Handbook of optics, geometrical and physical optics, polarized light, components and instruments. *McGraw-Hill Companies*, 1, 2010. 2

[5] D. Berman, T. Treibitz, and S. Avidan. Non-local image dehazing. In *IEEE CVPR*, 2016. 5, 6, 7, 8

[6] Noel Bonnet. Some trends in microscope image processing. *Micron Elsevier*, 2004. 2

[7] J. Boulanger, C. Kervrann, P. Bouthemy, P. Elbau, J.-B. Sibarita, and J. Salamero. Patch-based non-local functional for denoising fluorescence microscopy image sequences. *IEEE Trans. Med. Imag.*, 2010. 2

[8] A. Buades, B. Coll, and J. M. Morel. A review of image denoising methods, with a new one. *SIAM J. Multiscale Model. Simul.*, 2005. 2

[9] S. Cakir, D. C. Kahraman, R. Cetin-Atalay, and A. E. Cetin. Contrast enhancement of microscopy images using image phase information. *IEEE Access*, 6, 2018. 2

[10] P. M. Carlton et al. Fast live simultaneous multiwavelength four-dimensional optical microscopy. In *Proc. Nat. Acad. Sci.*, 2010. 2

[11] Xiaodong Chen, Bin Zheng, and Hong Liu. Optical and digital microscopic imaging techniques and applications in pathology. *Analytical Cellular Pathology*, 34, 2011. 2

[12] A. de Decker, J. A. Lee, and M. Verlysen. Variance stabilizing transformations in patch-based bilateral filters for poisson noise image denoising. In *Proc. IEEE Eng. Med. Biol. Soc. (EMBS)*, 2009. 2

[13] S. Dokudovskaya et al. A conserved coatomer-related complex containing sec13 and seh1 dynamically associates with the vacuole in saccharomyces cerevisiae. *Mol. Cell Proteomics*, 2011. 2

[14] D. L. Donoho and A. G. Flesia. Can recent innovations in harmonic analysis explain key findings in natural image statistics. *Net Comput Neural Sys*, 2001. 2

[15] S. P. Ehsani, H. S. Mousavi, and B. H. Khalaj. Chromosome image contrast enhancement using adaptive, iterative histogram matching. In *Iranian Conference on Machine Vision and Image Processing*, 2011. 2

[16] M. M. Frigault, J. Lacoste, J. L. Swift, and C. M. Brown. Live-cell microscopy - tips and tools. *Journal of Cell Science*, 2009. 1, 3, 8

[17] Xueyang Fu, Zhiwen Fan, Mei Ling, Yue Huang, and Xinghao Ding. Two-step approach for single underwater image enhancement. In *International Symposium on Intelligent Signal Processing and Communication Systems*, 2017. 5, 6

[18] Xueyang Fu, Delu Zeng, Yue Huang, Yinghao Liao, Xinghao Ding, and John Paisley. A fusion-based enhancing method for weakly illuminated images. *Signal Processing*, 2016. 5

[19] Gregory M. Galdino, Paul N. Manson, and Craig A. Vander Kolk. The digital darkroom, part 2: Digital photography basics. *Aesthetic Surgery*, 2000. 2

[20] D. Geman and Chengda Yang. Nonlinear image recovery with half-quadratic regularization. *IEEE Tran IP*, 1995. 4

[21] R. Giryes and M. Elad. Sparsity based poisson denoising. In *Proc. Elect. Electron. Eng. Israel (IEEEI)*, 2012. 2

[22] A. Gomez, L. Beltran del Rio, D. Romeu, and J. Yacaman. Application of the wavelet transform to the digital image processing of electron micrographs and of back reflection electron diffraction patterns. *Scanning Microscope*, 1992. 2

[23] H. Greenspan, B. van Ginneken, and R. M. Summers. Guest editorial deep learning in medical imaging: Overview and future promise of an exciting new technique. *IEEE Trans. Med. Imag.*, 2016. 1

[24] M. N. Gurcan, L. E. Boucheron, A. Can, A. Madabushi, N. M. Rajpoot, and B. Yener. Histopathological image analysis: A review. *IEEE Rev. Biomed. Eng.*, 2009. 1

[25] A. Hore and D. Ziou. Image quality metrics: Psnr vs. ssim. In *ICPR*, 2010. 5

[26] Xun Huang, Ming-Yu Liu, Serge Belongie, and Jan Kautz. Multimodal unsupervised image-to-image translation. In *ECCV*, 2018. 2

[27] M. J. Hytch and L. Potez. Geometric phase analysis of high resolution electron microscopy images of antiphase domains: example cu3au. *Philos. Mag.*, 1997. 2

[28] M. J. Hytch, E. Snoek, and R. Kilaas. Quantitative measurement of displacement and strain fields from hrem micrographs. *Ultramicroscopy*, 1998. 2

[29] Health Effects Institute. Airborne particles and health: Hei epidemiologic evidence. *HEI Perspectives, Cambridge*, 2001. 3

[30] S. Jeanson, J. Chaduf, M. N. Madec, S. Aly, J. Floury, T. F. Brocklehurst, and S. Lortal. Spatial distribution of bacterial colonies in a model cheese. *Applied and Environmental Microbiology*, 2011. 2

[31] H. Ernst Keller and S. Watkins. Contrast enhancement in light microscopy. *Curr Protoc Cytom.*, 2013. 2

[32] C. Kervrann, C. . S. Sorzano, S. T. Acton, J. Olivo-Marin, and M. Unser. A guided tour of selected image processing and analysis methods for fluorescence and electron microscopy. *IEEE Journal of Selected Topics in Signal Processing*, 10, 2016. 2

[33] Dilip Krishnan and Rob Fergus. Fast image deconvolution using hyper-laplacian priors. In *NIPS*, 2009. 4

[34] Hsin-Ying Lee, Hung-Yu Tseng, Jia-Bin Huang, Maneesh Kumar Singh, and Ming-Hsuan Yang. Diverse image-to-image translation via disentangled representations. In *European Conference on Computer Vision*, 2018. 2

[35] Hsin-Ying Lee, Hung-Yu Tseng, Qi Mao, Jia-Bin Huang, Yu-Ding Lu, Maneesh Kumar Singh, and Ming-Hsuan Yang. Drit++: Diverse image-to-image translation viadisentangled representations. *arXiv preprint arXiv:1905.01270*, 2019. 2

[36] Stamatis Lefkimmiatis. Universal denoising networks : A novel cnn architecture for image denoising. In *CVPR*. IEEE, 2018. 5, 6, 7, 8

[37] S. Lefkimmiatis and M. Unser. Poisson image reconstruction with hessian schatten-norm regularization. *IEEE Trans. Image Process.*, 2013. 2

[38] Anat Levin and Yair Weiss. User assisted separation of reflections from a single image using a sparsity prior. *IEEE Tran on Pattern Analysis and Machine Intelligence*, 29, 2007. 3

[39] Jinyou Liang. Chemical modeling for air resources: Fundamentals, applications, and corroborative analysis, 2013. Elsevier. 1, 3

[40] H. Liao, W. Lin, S. K. Zhou, and J. Luo. Adn: Artifact disentanglement network for unsupervised metal artifact reduction. *IEEE Transactions on Medical Imaging*, 2019. 2

[41] Haofu Liao, Wei-An Lin, Jianbo Yuan, S. Kevin Zhou, and Jiebo Luo. Artifact disentanglement network for unsupervised metal artifact reduction. In *MICCAI*, 2019. 2

[42] A. Matsuda, L. Shao, J. Boulanger, C. Kervrann, P. M. Carlton, P. Kner, E. Brandlund, D. Agard, and J. W. Sedat. Condensed mitotic chromosome structure at nanometer resolution using palm and egfp-histones. In *PLoS One*, 2010. 2

[43] M. T. McCann, J. A. Ozolek, C. A. Castro, B. Parvin, and J. Kovacevic. Automated histology analysis: Opportunities for signal processing. *IEEE Signal Process. Mag.*, 2015. 1

[44] Tobias Meyer, Michael Schmitt, and Jurgen Popp. Multimodal microscopy for tissue diagnostics. *Light Microscopy*, 2018. 2

[45] Michael J. Mobley. Photon diffraction described by momentum exchange theory: what more can edge diffraction tell us? In *SPIE Optical Engineering Applications,*, 2015. 4

[46] U. Nnolim and P. Lee. Homomorphic filtering of colour images using a spatial filter kernel in the hsi colour space. In *IEEE Instru and Measure. Tech Conf*, 2008. 5

[47] D. I. Pattison and M. J. Davies. Actions of ultraviolet light on cellular structures. *EXS*, 2006. 3, 5

[48] Wenqi Ren, Si Liu, Hua Zhang, Jinshan Pan, Xiaochun Cao, and Ming-Hsuan Yang. Single image dehazing via multi-scale convolutional neural networks. In *ECCV*, 2016. 5, 6

[49] A. E. Saliba et al. Microfluidic sorting and high content multimodal typing of cancer cells in self-assembled magnetic arrays. In *Proc. Nat. Acad. Sci.*, 2010. 2

[50] J. Salmon, C. A. Deledalle, R. Willett, and Z. T. Harmany. Poisson noise reduction with non-local pca. In *Proc. IEEE Int. Conf. Acoust., Speech, Signal Process. (ICASSP)*, 2012. 2

[51] F. Soulez. A learn 2d, apply 3d method for 3d deconvolution microscopy. In *Proc. IEEE Int. Symp. Biomed. Imag. (ISBI)*, 2014. 2

[52] H. Su, F. Xing, X. Kong, Y. Xie, S. Zhang, and L. Yang. Robust cell detection and segmentation in histopathological images using sparse reconstruction and stacked denoising autoencoders. In *Int. Conf. Med. Image Comput. Comput.-Assist. Intervent.*, 2015. 1

[53] Marshall F Tappen, William T Freeman, and Edward H Adelson. Recovering intrinsic images from a single image. *IEEE Transactions on Pattern Analysis and Machine Intelligence*, 27, 2005. 3

[54] Cover slip. `https://microscopy.duke.edu`. 3

[55] Triboelectric series. `http://soft-matter.seas.harvard.edu`. 3

[56] Robert K Tyson. *Principles and Applications of Fourier Optics*. IOP Publishing, Bristol, UK, 2014. 4

[57] Thibault Vaillant de Gulis, Alfons Schwarzenboeck, Valery Shcherbakov, Christophe Gourbeyre, Bastien Laurent, Regis Dupuy, Pierre Coutris, and Christophe Duroure. Study of the diffraction pattern of cloud particles and respective response of optical array probes. *Atmospheric Measurement Techniques Discussions*, 2018. 4

[58] Claudio Vinegoni, Tyler Ralston, Wei Tan, Wei Luo, Daniel L. Marks, and Stephen A. Boppart. Multi-modality imaging of structure and function combining spectral-domain optical coherence and multiphoton microscopy. *International Society for Optical Engineering*, 2006. 2

[59] C. S. Wong, I. Robinson, MA Ochsenkhn, J Arlt, WJ Hossack, and J Crain. Changes to lipid droplet configuration in mcmv-infected fibroblasts: live cell imaging with simultaneous cars and two-photon fluorescence microscopy. *Biomed Opt Express.*, 2011. 2

[60] Qiang Wu, Fatima A. Merchant, and Kenneth R. Castleman. Microscope image processing. *Elsevier Book*, 2008. 2

[61] W. Xie, J. A. Noble, and A. Zisserman. Microscopy cell counting with fully convolutional regression networks. In *Workshop Deep Learn. Med. Image Anal. (MICCAI)*, 2015. 1

[62] Fuyong Xing, Yuanpu Xie, Hai Su, Fujun Liu, and Lin Yang. Deep learning in microscopy image analysis: A survey. *IEEE Tran Neural Net and Learning Sys*, 29, 2018. 1

[63] F. Xing, Y. Xie, and L. Yang. An automatic learning-based framework for robust nucleus segmentation. *IEEE Trans. Med. Imag.*, 2016. 1

[64] F. Xing and L. Yang. Robust nucleus/cell detection and segmentation in digital pathology and microscopy images: A comprehensive review. *IEEE Rev. Biomed. Eng.*, 2016. 1

[65] Jun Xu, Lei Zhang, and David Zhang. A trilateral weighted sparse coding scheme for real-world image denoising. *ECCV*, 2018. 5, 6, 7, 8

[66] CC. Yang. Image enhancement by adjusting the contrast of spatial frequencies. *Optik*, 2008. 2

[67] Shenglan Zhang, Xufei Qian, A. Gupta, and M. E. Martone. A practical approach for microscopy imaging data management (midm) in neuroscience. In *15th International Conference on Scientific and Statistical Database Management*, 2003. 1

[68] Youbo Zhao, Benedikt W. Graf, Eric J. Chaney, Ziad Mahmassani, Eleni Antoniadou, Ross DeVolder, Hyunjoon Kong, Marni D. Boppart, , and Stephen A. Boppart. Integrated multimodal optical microscopy for structural and functional imaging of engineered and natural skin. *Journal of biophotonics*, 2012. 2

[69] Karel Zuiderveld. Graphics gems iv. chapter Contrast Limited Adaptive Histogram Equalization. Academic Press Professional, Inc., 1994. 5, 6, 7, 8